Quantum Interference between Photons from an Atomic Ensemble and a Remote Atomic Ion

A. N. Craddock,[1,†] J. Hannegan,[1,†] D. P. Ornelas-Huerta,[1] J. D. Siverns,[1] A. J. Hachtel,[1] E. A. Goldschmidt,[2] J. V. Porto,[1] Q. Quraishi,[2,1] and S. L. Rolston[1,*]

[1]*Joint Quantum Institute, National Institute of Standards and Technology and the University of Maryland, College Park, Maryland 20742, USA*

[2]*Army Research Laboratory, 2800 Powder Mill Road, Adelphi, Maryland 20783, USA*

(Received 30 July 2019; published 18 November 2019)

Many remote-entanglement protocols rely on the generation and interference of photons produced by nodes within a quantum network. Quantum networks based on heterogeneous nodes provide a versatile platform by utilizing the complementary strengths of the differing systems. Implementation of such networks is challenging, due to the disparate spectral and temporal characteristics of the photons generated by the different quantum systems. Here, we report on the observation of quantum interference between photons generated from a single ion and an atomic ensemble. The photons are produced on demand by each source located in separate buildings, in a manner suitable for quantum networking. Given these results, we analyze the feasibility of hybrid ion-ensemble remote entanglement generation.

DOI: 10.1103/PhysRevLett.123.213601

Advances in the distribution of quantum information will likely require entanglement shared across a hybrid quantum network [1–3]. The complementary strengths and functions of the different quantum systems give heterogeneous networks an advantage over those consisting of identical nodes. Many protocols for generating remote entanglement require interference between photons produced by the different network nodes, which has largely prevented investigations into photonic-based hybrid entanglement, owing to the large differences in the spectral characteristics of single photons generated by different quantum systems [1,4,5]. Although this is not a physical limitation [6,7], vanishing entanglement generation rates, along with the necessity for detectors with bandwidths orders of magnitude greater than currently available, has prohibited the linking of heterogeneous systems. Overcoming this spectral disparity will allow for the construction of hybrid networks with practical entanglement rates and expanded capabilities compared to networks based only on homogeneous components [1].

Two of the leading systems in the field of quantum information are Rydberg atoms and trapped ions. The strong optical nonlinearity exhibited by neutral-atom Rydberg ensembles enables the construction of single-photon sources [8], gates [9], and transistors [10]. Strong light-matter interactions make them well suited as quantum memories [11], and for implementing quantum repeaters [12,13]. Furthermore, arrays of Rydberg atoms are a powerful new platform for quantum simulation [14,15]. Trapped ions are leading candidates for quantum computation, communication, and simulation with good matter-to-photon conversion [16–23]. Their continued success owes to long coherence and trapping lifetimes [20], high fidelity operations [21], and ease of generating ion-photon entanglement [22,23].

In this work, we achieve high-visibility Hong-Ou-Mandel (HOM) interference [24] between photons generated from a rubidium atomic ensemble and a trapped barium ion after closely matching their center frequencies via difference frequency generation (DFG) [25]. This demonstration of interference between photons produced by these two systems is a critical step toward their remote entanglement. From our results we investigate the feasibility of hybrid ion-atomic ensemble remote entanglement generation, demonstrating that a hybrid ion-atomic ensemble quantum network is attainable.

Our experiment spans two buildings, shown in Fig. 1. Building *A* contains a single trapped $^{138}Ba^{+}$ ion as well as two DFG setups. Building *B* contains a ^{87}Rb atomic ensemble and a HOM interferometer to measure two-photon interference. A time-tagging device records detection events for two single-photon avalanche photodetectors (SPADs), *A* and *B*. Each building contains a Hanbury Brown–Twiss [26,27] setup (not pictured) for measurement of the second-order intensity autocorrelation functions, $g^{(2)}_{\mathrm{ion}}(\tau)$ and $g^{(2)}_{\mathrm{atom}}(\tau)$, of the light from ion and atomic-ensemble sources, respectively.

The ion emits single photons near 493 nm via spontaneous emission from the $6P_{1/2}$ excited state to the $6S_{1/2}$ ground state. A lens collects these photons (≈4% efficiency), and couples them (≈30% efficiency) into a single-mode fiber (SMF) connected to DFG-1, described in Ref. [25]. We spatially overlap these photons with a strong 1343-nm pump and couple both into a periodically poled lithium niobate waveguide. Here, DFG converts the

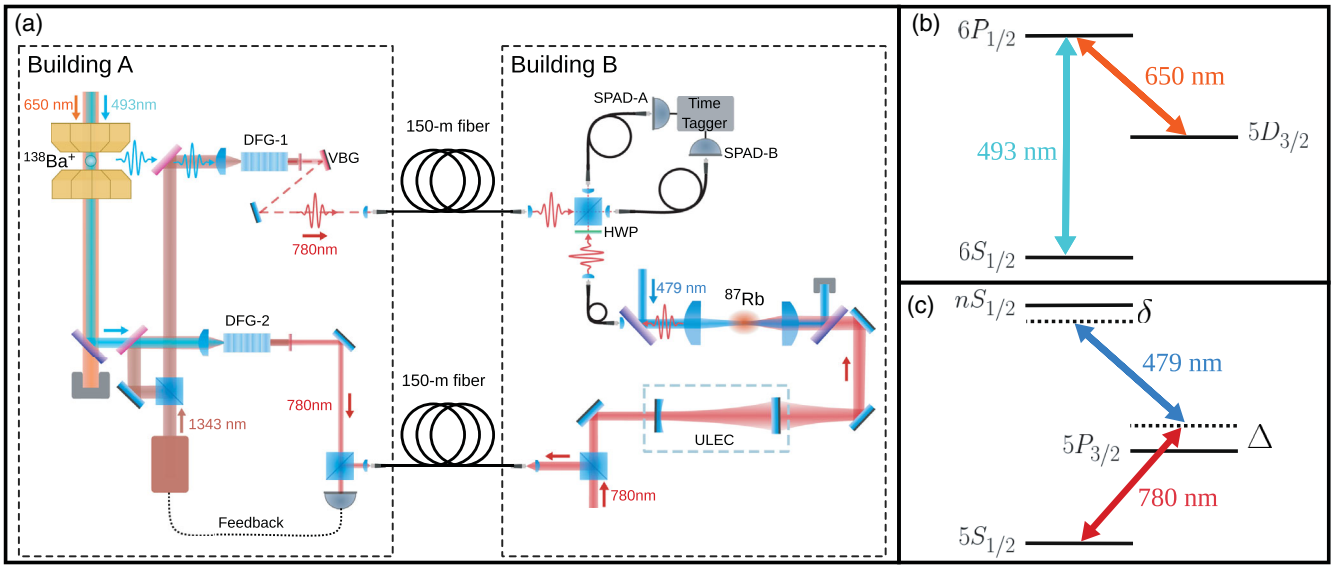

FIG. 1. Experimental layout and energy level diagrams for the two sources. (a) Building A contains a $^{138}Ba^{+}$ ion which emits photons at 493 nm, and building B contains a ^{87}Rb atomic ensemble producing 780-nm photons. Ion-emitted photons are converted to 780 nm using DFG-1 and sent to building B via PMF. DFG-2 produces 780-nm light used to frequency stabilize the output of DFG-1 by optical beat note locking with reference light sent from building B. Light from the ion and ensemble source is sent to the HOM interferometer for two-photon interference measurements. A half-wave plate (HWP) in one input path allows for control of the relative polarization of the photons. The photons interfere on a nearly 50:50 beam splitter before being coupled into two SMFs which are connected to SPADs linked to a time-tagging device. Here VBG stands for a volume Bragg grating and ULEC for ultralow expansion cavity. (b) Level scheme for $^{138}Ba^{+}$. (c) Level scheme for ^{87}Rb.

493-nm photons to 780 nm, while preserving their quantum statistics [25,28]. In addition to converted single photons, the pump light produces noise at longer wavelengths than the pump due to effects such as spontaneous down-conversion and Raman scattering, and noise near 780 nm due mainly to anti-Stokes Raman scattering. After filtering out this pump induced noise [29] to a rate negligible compared to the dark count rate of the SPADs, we send the converted photons to the HOM interferometer in building B via a 150-m polarization-maintaining fiber (PMF). To ensure the center frequency of the photons produced by DFG-1 matches that of the atomic ensemble, DFG-2 is used in an optical beat note lock setup which feeds back to the pump laser, where 780-nm light from building B acts as a reference.

The atomic-ensemble source uses Rydberg blockade [30] to produce single photons from an ensemble of cold ^{87}Rb atoms that are held in an optical dipole trap [10,31]. The ground $|5S_{1/2}, F=2, m_F=2\rangle$ and Rydberg $|nS_{1/2}, J=1/2, m_J=1/2\rangle$ states are coupled using a two-photon transition, via an intermediate state $|5P_{3/2}, F=3, m_F=3\rangle$, shown in Fig. 1(c), using 780-nm probe and counterpropagating 479-nm control fields. The probe light that has passed through the cloud is collected and coupled (≈70% efficiency) into a PMF. We operate with Rydberg levels with principal quantum numbers, $n \geq 120$, where the blockade radius is significantly larger than the probe beam waist, making the medium effectively one dimensional [31]. The atomic ensemble has a lifetime of ≈1 s, limited by the background vapor pressure. Thus, to maintain reasonable atom numbers over the course of the measurements, we periodically reload the ensemble.

First we consider the case where each source continuously produces single photons with stochastic arrival times. To produce these photons from the ion, we continuously Doppler cool on the $6S_{1/2} - 6P_{1/2}$ transition, repumping with 650-nm light; see Fig. 1(b). The emitted photons have a frequency spectrum centered on the cooling laser frequency, and with a shape determined by the Rabi frequencies and detunings of both the cooling and repumping lasers [32]. The average count rate of converted photons throughout the experiment R_{ion} measured as the sum of counts on SPAD A and B in building B, is ≈400 s^{-1}. Figure 2(a) shows $g^{(2)}_{\mathrm{ion}}(\tau)$ for the resulting 780-nm photon stream. We measure $g^{(2)}_{\mathrm{ion}}(0) = 0.05(8)$ after background subtraction. Here, the $g^{(2)}_{\mathrm{ion}}$ dip width is set by the effective Rabi frequency ($\approx 2\pi \times 100$ MHz) of the driving 493-nm light, which additionally dictates the emitted photon's bandwidth.

To produce a stochastic photon stream from the atomic ensemble source, we tune the probe and control fields to their respective atomic resonances, $\Delta = \delta = 0$; see Fig. 1(c). The strong nonlinearities associated with Rydberg electromagnetically induced transparency (REIT) ensures that only single photons propagate through the medium without large

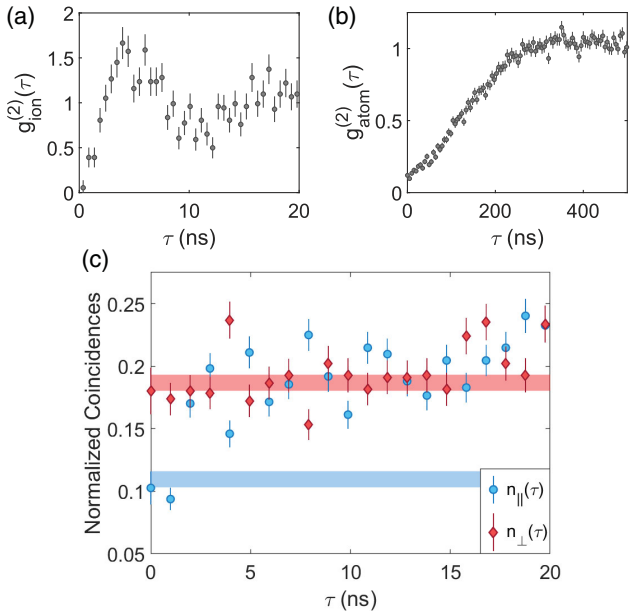

FIG. 2. Data for stochastic photon production and interference. Second-order intensity autocorrelation functions for the (a) ion source and (b) atomic-ensemble source. The oscillation exhibited in the ion autocorrelation data is attributed to Rabi flopping of the ion. (c) Normalized coincidences for the cases where the relative polarization of the two sources at the interferometer are parallel, $n_{\parallel}(\tau)$, and perpendicular, $n_{\perp}(\tau)$, using 1-ns bins. Lower (blue) [upper (red)] band corresponds to the expected normalized coincidences when photons from the sources are completely indistinguishable [distinguishable]. For the lower (blue) band expected coincidences are entirely due to atomic-ensemble source multiphoton events, while for the upper (red) band there is an additional contribution from photon distinguishability. Bands indicate the $\pm 1\sigma$ confidence interval in this value due to the uncertainty in $g^{(2)}_{\mathrm{atom}}(0)$. Data shown accumulated in ≈30 h. In all cases the error bars denote statistical uncertainties. All curves shown include background subtraction. Raw two-photon interference data and calculation of expected coincidence bands can be found in Ref. [33].

losses [31]. In steady-state operation at a high Rydberg level, $n = 120$, and large optical depth, OD ≈ 30, we observe a background-subtracted $g^{(2)}_{\mathrm{atom}}(0) = 0.119(7)$, shown in Fig. 2(b). We attribute the nonzero value of $g^{(2)}_{\mathrm{atom}}(0)$ to finite probe beam size and input photon flux effects [31,47]. The width of the $g^{(2)}_{\mathrm{atom}}$ dip is set by the REIT bandwidth [31]. However, the majority of the photons exiting the medium have similar spectral bandwidths to the input probe field [48]. We measure an average photon count rate throughout the experiment, R_{atom}, of $\approx 10^4$ s^{-1}, with an experimental duty cycle of 0.56, where the off time is used for reloading.

The background-subtracted normalized coincidences for the HOM interference are shown in Fig. 2(c) for the cases where the relative polarization at the interferometer of the photons from the two sources are parallel, $n_{\parallel}(\tau)$, and perpendicular, $n_{\perp}(\tau)$. The subtracted background is predominantly due to SPAD dark counts and ambient photons. We define the visibility of the interference,

$$V = \frac{n_{\perp}(0) - n_{\parallel}(0)}{n_{\perp}(0)}, \tag{1}$$

and observe $V = 0.43(9)$ using 1-ns bins. For a perfect 50:50 beam splitter two factors can contribute to a nonunity visibility: multiphoton events from either of the sources, quantified by $g^{(2)}(0)$, and distinguishability. Multiphoton events decrease the visibility by a factor

$$f_{\mathrm{mp}} = \left(1 + \frac{r g^{(2)}_{\mathrm{atom}}(0) + r^{-1} g^{(2)}_{\mathrm{ion}}(0)}{2}\right)^{-1}, \tag{2}$$

where $r = R_{\mathrm{atom}}/R_{\mathrm{ion}}$. Equation (2) holds for the case where the photon flux is constant over the experiment, which is a valid approximation for these data [33]. Given the independently measured $g^{(2)}(0)$ for the sources and ratio r, we determine $f_{\mathrm{mp}} = 0.41(1)$. The observed 0.43(9) visibility can thus be attributed entirely to multiphoton events, and therefore is consistent with perfect bunching of photons from the two sources. Additionally, we note that $n_{\parallel}(0)$ and $n_{\perp}(0)$ are in agreement with the values expected from the measured $g^{(2)}(0)$'s, shown in Fig. 2(c). Because of the disparity in the spectral widths of the photons produced by the sources, the width of the HOM dip, seen in Fig. 2(c), is almost entirely determined by the temporally narrower ion-produced photon.

To be useful for quantum networking, the photons should arrive on demand in well-defined temporal modes [49]. To this end, we investigate two-photon interference in the case where a single photon from each source arrives at a known time relative to an experimental trigger shared between the two buildings.

To produce on-demand single photons from the ion, we first prepare it in the $5D_{3/2}$ manifold via optical pumping using 493-nm light. A pulse of 650-nm light then excites to the $6P_{1/2}$ manifold, from which decay to the $6S_{1/2}$ ground manifold produces a single 493-nm photon [50], with measured $g^{(2)}_{\mathrm{ion}}(0) = 0(1) \times 10^{-2}$ after background subtraction. We detect a photon at the output of the HOM interferometer with a probability of $\approx 2 \times 10^{-5}$ per attempt. Photons are emitted from the ion with a nearly exponential decaying temporal profile, with a decay constant (≈50 ns) set by the effective Rabi frequency of the 650-nm retrieval pulse. Because of the magnetic bias field (≈5 G) splitting the Zeeman states in the $6S_{1/2}$ and $5D_{3/2}$ levels, combined with technical limitations resulting in a near-equal population distribution in the $5D_{3/2}$ manifold following pumping, the average photon spectrum consists of several peaks with a center frequency determined by the detuning of the 650-nm laser used to excite the ion from the $5D_{3/2} - 6P_{1/2}$ transition [33].

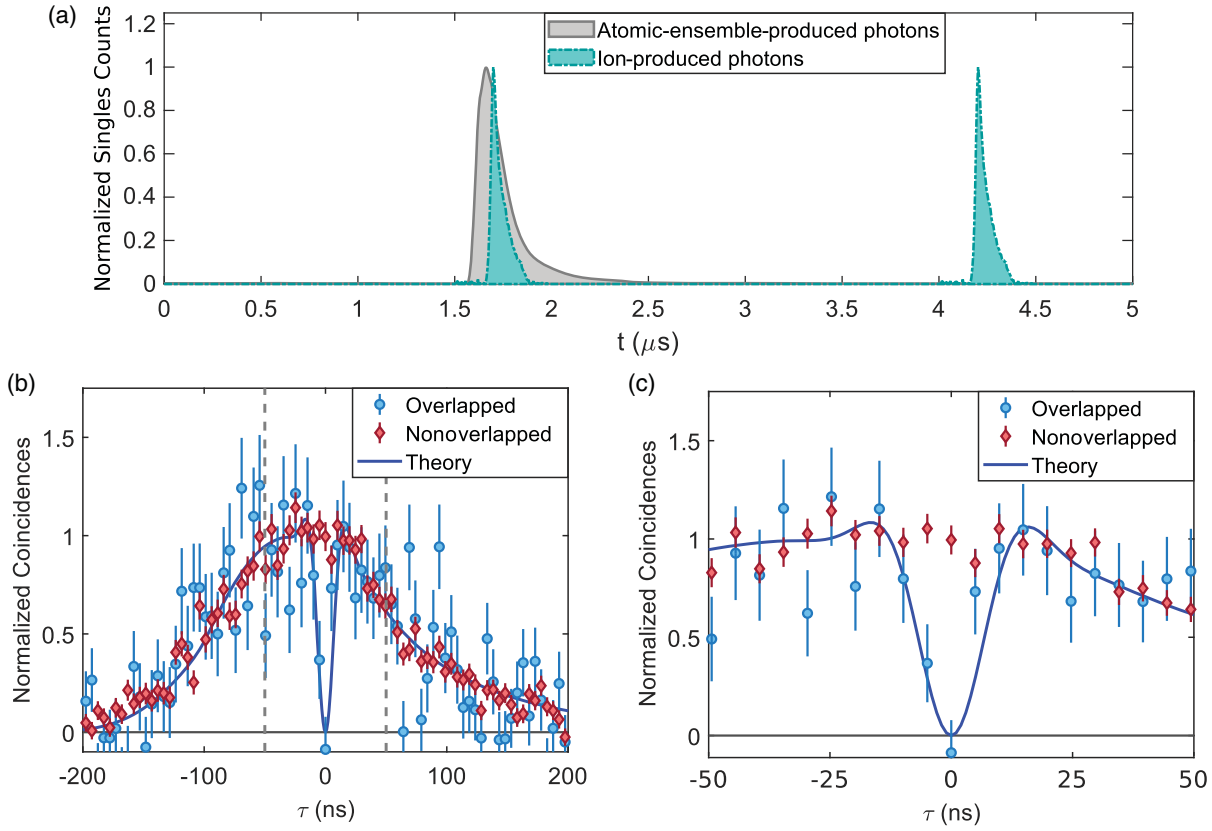

FIG. 3. On-demand pulse sequence and interference. (a) Schematic of pulse sequence for one period. The atomic-ensemble-produced photon profile, and ion-produced photon profile at $t \approx 4.25$ μs, are measured directly. The ion-produced photon profile at $t \approx 1.75$ μs is a time shifted copy of that at $t \approx 4.25$ μs to allow for easy comparison of the photon temporal shapes from the two sources. To lessen the effects of small drifts in the relative arrival time of the photons, we offset the ion- and atomic-ensemble-produced photon average arrival times. (b),(c) Normalized coincidences when the photons from the two sources are temporally overlapped (nonoverlapped) shown in blue (red). Both curves represent the data after software gating, background subtraction, and using 5-ns bins. Dashed lines in (b) indicate the range shown in (c). Theory curve obtained taking into account the nontransform limited nature, probabilistic spectrum of the ion-produced photon, and plausible estimates of the relative drift ($2\pi \times 10$ MHz) and offset ($2\pi \times 20$ MHz) between the center frequencies of the photons from the two sources. Data presented accumulated over ≈22 h. In all cases the error bars denote statistical uncertainties. Raw two-photon interference data and calculation of theory curves can be found in Ref. [33].

For the atomic-ensemble source, we generate on-demand photons using a write and retrieve protocol, similar to that in Ref. [8]. A Rydberg collective spin wave excitation is written to the cloud using coherent control and probe pulses, detuned far from intermediate resonance ($\Delta \gg \Gamma$, the linewidth of the intermediate state) and close to two-photon resonance ($\delta = 0$). Rydberg blockade during the write process ensures that a single Rydberg spin wave excitation is stored in the medium. The control field is tuned close to resonance and then turned on, retrieving the spin wave as a single photon with a spatial mode similar to the input probe light. After accounting for background coincidences, we measure $g^{(2)}_{\mathrm{atom}}(0) = 0(1) \times 10^{-4}$, with a per-attempt detection probability $\approx 3 \times 10^{-2}$ at the outputs of the HOM interferometer. The temporal profile of the retrieved photon is determined by the control Rabi frequency ($\approx 2\pi \times 7$ MHz), intermediate state detuning ($\approx 2\pi \times 7$ MHz), and optical depth (≈10) of the cloud [51]. Figure 3(a) shows the temporal profile of the atomic-ensemble-produced photon, well approximated by a decaying exponential, with a decay constant ≈120 ns.

To measure the visibility in a single experimental run, instead of using polarization to make the photons distinguishable, we use a procedure where the ion-produced photons alternately arrive simultaneously on the beam splitter with the atomic-ensemble-produced photons (with identical polarization), interleaved with pulses when their arrival times are not overlapped, depicted in Fig. 3(a). We use coincidences across several shifted arrival times to correspond to our orthogonal mode reference, to improve statistical noise [33]. Our experimental sequence consists of requesting photons from the atomic ensemble at a rate of 200 kHz, while the ion produces photons at 400 kHz, triggered via an optical link between the buildings. We offset the average arrival times of the ion- and atomic-ensemble-produced photons to mitigate the effects of the small drifts in the relative arrival time of the two sources.

We operate at an experimental duty cycle of 0.6, with the non-data-taking time required to reload the atomic ensemble.

To mitigate noise effects, predominantly due to detector dark counts and ambient photons, we software gate SPAD A using a 120-ns time window containing ≈80% of the ion-produced photon temporal profile. With this gating, we count the coincidences in detection events between SPAD A and B. Figures 3(b) and 3(c) show the resulting data for 5-ns bins after subtraction of background coincidences and software gating. Using Eq. (1), where $n_{\parallel}$ and $n_{\perp}$ correspond to the temporally overlapped and nonoverlapped coincidences, respectively, we calculate a visibility of 1.1(2). The observed width of the interference dip is narrower than expected when only considering the temporal profile of the photons [6]. However, accounting for the multiple peaks in the ion-produced photon spectra, reasonable laser-frequency drifts, and average center-frequency differences of the two photons, we obtain agreement between theory and experiment, shown in Figs. 3(b) and 3(c). Details on how the various phenomena affect the interference dip can be found in Ref. [33].

Having observed interference between photons generated from two fundamentally different quantum sources, we now examine our results in the context of hybrid quantum networking. We consider the entanglement generation scheme in Refs. [5,22] as a natural extension of our setup to create a Bell-state analyzer, enabling the heralded generation of maximally entangled matter qubits. With this scheme, the resulting state fidelity, assuming perfect photon-matter entanglement and polarization discrimination, can be related to the visibility of the two-photon interference $F = (1 + V)/2$ [33]. For the 5-ns bins in Fig. 3(c), we project $F \approx 1$. With the measured ≈40 bunching events and ≈21 h experimental run time, we infer an entanglement rate of ≈2 h^{-1}. These calculations assume negligible detector dark counts, achievable with commercially available detectors and through improved shielding of the detectors from ambient photon sources. Compromising by using a larger bin we can increase the entanglement rate while decreasing the fidelity [7]. For example, with 10-ns bins we estimate an entanglement rate of ≈4 h^{-1} with $F \approx 0.9$, still well above the classical limit. Such entanglement rates are comparable with the first experiments using similar schemes with homogeneous matter qubits [52,53]. Additionally, we note that with reasonable improvements to photon collection and detection, entanglement generation rates on the order of several events per minute, with $F > 0.9$, are achievable. These improvements are discussed in further detail in Ref. [33].

In conclusion, we have demonstrated high-visibility quantum interference between photons produced by an ion and atomic ensemble in both the stochastic and on-demand regime. With the current configuration, we project that entanglement rates of ≈2 h^{-1} are achievable. With practical experimental upgrades, predominantly improving the ion-produced photon collection, DFG conversion efficiency, and reducing optical losses through various elements, this can be increased to several entanglement events per minute, making the construction of a hybrid ion-atomic ensemble quantum network practical.

All authors acknowledge support from the U.S. Army Research Lab's Center for Distributed Quantum Information (CDQI) at the University of Maryland and the Army Research Lab. A. N. C., D. P. O.-H, A. J. H., S. L. R., and J. V. P. additionally acknowledge support from the National Science Foundation Physics Frontier Center at the Joint Quantum Institute (Grant No. PHY1430094).

*Corresponding author.
rolston@umd.edu
†J. H. and A. N. C. contributed equally to this work.

[1] N. Maring, P. Farrera, K. Kutluer, M. Mazzera, G. Heinze, and H. de Riedmatten, Nature (London) **551**, 485 (2017).
[2] M. Lettner, M. Mücke, S. Riedl, C. Vo, C. Hahn, S. Baur, J. Bochmann, S. Ritter, S. Dürr, and G. Rempe, Phys. Rev. Lett. **106**, 210503 (2011).
[3] H. M. Meyer, R. Stockill, M. Steiner, C. Le Gall, C. Matthiesen, E. Clarke, A. Ludwig, J. Reichel, M. Atatüre, and M. Köhl, Phys. Rev. Lett. **114**, 123001 (2015).
[4] N. Sangouard, C. Simon, H. de Riedmatten, and N. Gisin, Rev. Mod. Phys. **83**, 33 (2011).
[5] C. Simon and W. T. M. Irvine, Phys. Rev. Lett. **91**, 110405 (2003).
[6] T. Legero, T. Wilk, A. Kuhn, and G. Rempe, Appl. Phys. B **77**, 797 (2003).
[7] A. M. Dyckovsky and S. Olmschenk, Phys. Rev. A **85**, 052322 (2012).
[8] Y. O. Dudin and A. Kuzmich, Science **336**, 887 (2012).
[9] J. D. Thompson, T. L. Nicholson, Q.-Y. Liang, S. H. Cantu, A. V. Venkatramani, S. Choi, I. A. Fedorov, D. Viscor, T. Pohl, M. D. Lukin, and V. Vuletić, Nature (London) **542**, 206 (2017).
[10] H. Gorniaczyk, C. Tresp, J. Schmidt, H. Fedder, and S. Hofferberth, Phys. Rev. Lett. **113**, 053601 (2014).
[11] J. Lampen, H. Nguyen, L. Li, P. R. Berman, and A. Kuzmich, Phys. Rev. A **98**, 033411 (2018).
[12] N. Solmeyer, X. Li, and Q. Quraishi, Phys. Rev. A **93**, 042301 (2016).
[13] B. Zhao, M. Müller, K. Hammerer, and P. Zoller, Phys. Rev. A **81**, 052329 (2010).
[14] S. de Léséleuc, S. Weber, V. Lienhard, D. Barredo, H. P. Büchler, T. Lahaye, and A. Browaeys, Phys. Rev. Lett. **120**, 113602 (2018).
[15] H. Bernien, S. Schwartz, A. Keesling, H. Levine, A. Omran, H. Pichler, S. Choi, A. S. Zibrov, M. Endres, M. Greiner, V. Vuletic, and M. D. Lukin, Nature (London) **551**, 579 (2017).
[16] C. Figgatt, D. Maslov, K. Landsman, N. M. Linke, S. Debnath, and C. Monroe, Nat. Commun. **8**, 1918 (2017).
[17] H. Häffner, C. F. Roos, and R. Blatt, Phys. Rep. **469**, 155 (2008).

[18] R. Blatt and C. F. Roos, Nat. Phys. **8**, 277 (2012).
[19] J. Zhang, G. Pagano, P. W. Hess, A. Kyprianidis, P. Becker, H. Kaplan, A. V. Gorshkov, Z.-X. Gong, and C. Monroe, Nature (London) **551**, 601 (2017).
[20] C. Langer, R. Ozeri, J. D. Jost, J. Chiaverini, B. DeMarco, A. Ben-Kish, R. B. Blakestad, J. Britton, D. B. Hume, W. M. Itano *et al.*, Phys. Rev. Lett. **95**, 060502 (2005).
[21] T. P. Harty, D. T. C. Allcock, C. J. Ballance, L. Guidoni, H. A. Janacek, N. M. Linke, D. N. Stacey, and D. M. Lucas, Phys. Rev. Lett. **113**, 220501 (2014).
[22] D. Hucul, I. V. Inlek, G. Vittorini, C. Crocker, S. Debnath, S. M. Clark, and C. Monroe, Nat. Phys. **11**, 37 (2015).
[23] M. Bock, P. Eich, S. Kucera, M. Kreis, A. Lenhard, C. Becher, and J. Eschner, Nat. Commun. **9**, 1998 (2018).
[24] C. K. Hong, Z. Y. Ou, and L. Mandel, Phys. Rev. Lett. **59**, 2044 (1987).
[25] J. D. Siverns, J. Hannegan, and Q. Quraishi, Phys. Rev. Applied **11**, 014044 (2019).
[26] R. Hanbury Brown and R. Q. Twiss, Nature (London) **177**, 27 (1956).
[27] H. J. Kimble, M. Dagenais, and L. Mandel, Phys. Rev. Lett. **39**, 691 (1977).
[28] P. Kumar, Opt. Lett. **15**, 1476 (1990).
[29] J. D. Siverns, J. Hannegan, and Q. Quraishi, Sci. Adv **5**, eaav4651 (2019).
[30] E. Urban, T. A. Johnson, T. Henage, L. Isenhower, D. Yavuz, T. Walker, and M. Saffman, Nat. Phys. **5**, 110 (2009).
[31] T. Peyronel, O. Firstenberg, Q.-Y. Liang, S. Hofferberth, A. V. Gorshkov, T. Pohl, M. D. Lukin, and V. Vuletić, Nature (London) **488**, 57 (2012).
[32] Y. Stalgies, I. Siemers, B. Appasamy, T. Altevogt, and P. Toschek, Europhys. Lett. **35**, 259 (1996).
[33] See Supplemental Material at http://link.aps.org/supplemental/10.1103/PhysRevLett.123.213601 for further details on experimental setups, analytical methods used to produce Fig. 3, derivation of Eq. (2), and calculation of theory curve in Fig. 3, which includes Refs. [34–46].
[34] J. D. Siverns and Q. Quraishi, Quantum Inf. Process. **16**, 314 (2017).
[35] D. Eger, M. Arbore, M. Fejer, and M. Bortz, J. Appl. Phys. **82**, 998 (1997).
[36] O. Kashin, M. Homann, V. Matusevich, F. Setzpfandt, T. Pertsch, and R. Kowarschik, Appl. Phys. B **104**, 547 (2011).
[37] T. Fujiwara, X. Cao, R. Srivastava, and R. V. Ramaswamy, Appl. Phys. Lett. **61**, 743 (1992).
[38] D. Boiron, C. Triché, D. R. Meacher, P. Verkerk, and G. Grynberg, Phys. Rev. A **52**, R3425 (1995).
[39] S. de Léséleuc, D. Barredo, V. Lienhard, A. Browaeys, and T. Lahaye, Phys. Rev. A **97**, 053803 (2018).
[40] P. Bienias, Eur. Phys. J. Spec. Top. **225**, 2957 (2016).
[41] M. Saffman, T. G. Walker, and K. Mølmer, Rev. Mod. Phys. **82**, 2313 (2010).
[42] M. Stevens, *Single-Photon Generation and Detection: Physics and Applications* (Academic Press, New York, 2013), Chap. 2, pp. 25–68.
[43] P. Müller, T. Tentrup, M. Bienert, G. Morigi, and J. Eschner, Phys. Rev. A **96**, 023861 (2017).
[44] S. Olmschenk, D. Hayes, D. N. Matsukevich, P. Maunz, D. L. Moehring, and C. Monroe, Int. J. Quantum. Inform. **08**, 337 (2010).
[45] V. Krutyanskiy, M. Meraner, J. Schupp, and B. P. Lanyon, Appl. Phys. B **123**, 228 (2017).
[46] M. Ghadimi, V. Blūms, B. G. Norton, P. M. Fisher, S. C. Connell, J. M. Amini, C. Volin, H. Hayden, C.-S. Pai, D. Kielpinski *et al.*, npj Quantum Inf. **3**, 4 (2017).
[47] P. Bienias, J. Douglas, A. Paris-Mandoki, P. Titum, I. Mirgorodskiy, C. Tresp, E. Zeuthen, M. J. Gullans, M. Manzoni, S. Hofferberth, D. Chang, and A. V. Gorshkov, arXiv:1807.07586.
[48] E. Zeuthen, M. J. Gullans, M. F. Maghrebi, and A. V. Gorshkov, Phys. Rev. Lett. **119**, 043602 (2017).
[49] M. Aspelmeyer, T. Jennewein, M. Pfennigbauer, W. R. Leeb, and A. Zeilinger, IEEE J. Sel. Top. Quantum Electron. **9**, 1541 (2003).
[50] J. D. Siverns, X. Li, and Q. Quraishi, Appl. Opt. **56**, B222 (2017).
[51] A. V. Gorshkov, A. André, M. Fleischhauer, A. S. Sørensen, and M. D. Lukin, Phys. Rev. Lett. **98**, 123601 (2007).
[52] D. L. Moehring, P. Maunz, S. Olmschenk, K. Younge, D. Matsukevich, L.-M. Duan, and C. Monroe, Nature (London) **449**, 68 (2007).
[53] D. N. Matsukevich, P. Maunz, D. L. Moehring, S. Olmschenk, and C. Monroe, Phys. Rev. Lett. **100**, 150404 (2008).